ORIGINAL PAPER

Estimating external tissue support parameters with fluid–structure interaction models from 4D ultrasound of murine thoracic aortae

Tanmay C. Shidhore[1] · Hannah L. Cebull[2] · Megan C. Madden[1] · Ivan C. Christov[1] · Vitaliy L. Rayz[1,2] · Craig J. Goergen[2]

Abstract

Modeling of fluid–structure interactions (FSIs) between the deformable arterial wall and blood flow is necessary to obtain physiologically realistic computational models of cardiovascular systems. However, lack of information on the nature of contact between the outer vessel wall and surrounding tissue presents challenges in prescribing appropriate structural boundary conditions. Imaging techniques used to visualize wall deformation in vivo may be useful for estimating simulation parameters that capture the effects of both vascular composition and surrounding tissue support on the vessel wall displacement. Here, we present a method to calibrate external tissue support parameters in FSI simulations against four-dimensional ultrasound (4DUS) of the murine thoracic aortae. We collected ultrasound, blood pressure, and histological data from several mice infused with angiotensin II ($n = 4$) and created a representative model of healthy and diseased (at 28 days post-angiotensin II infusion) murine aortae. We ran pulsatile FSI simulations after accounting for increased arterial wall stiffness with varying levels of tissue support, which demonstrated non-trivial variation in not only structural quantities, such as vessel wall deformation, but also hemodynamic quantities, such as wall shear stress across simulations. Furthermore, we compared simulation results with in vivo 4DUS imaging data and observed that the suitable range of the tissue support spring parameter was identical for both healthy and diseased states. This indicated that the same tissue support parameter estimates could be used for modeling the healthy and diseased states of the vessel, provided that changes in arterial wall stiffness had been considered. We anticipate this technique and the tissue support estimates reported herein will help inform computational models of blood flow and vasculature that incorporate the influence of external tissue.

Tanmay C. Shidhore and Hannah L. Cebull have contributed equally to this work.

✉ Craig J. Goergen
cgoergen@purdue.edu

Tanmay C. Shidhore
tshidhor@purdue.edu

Hannah L. Cebull
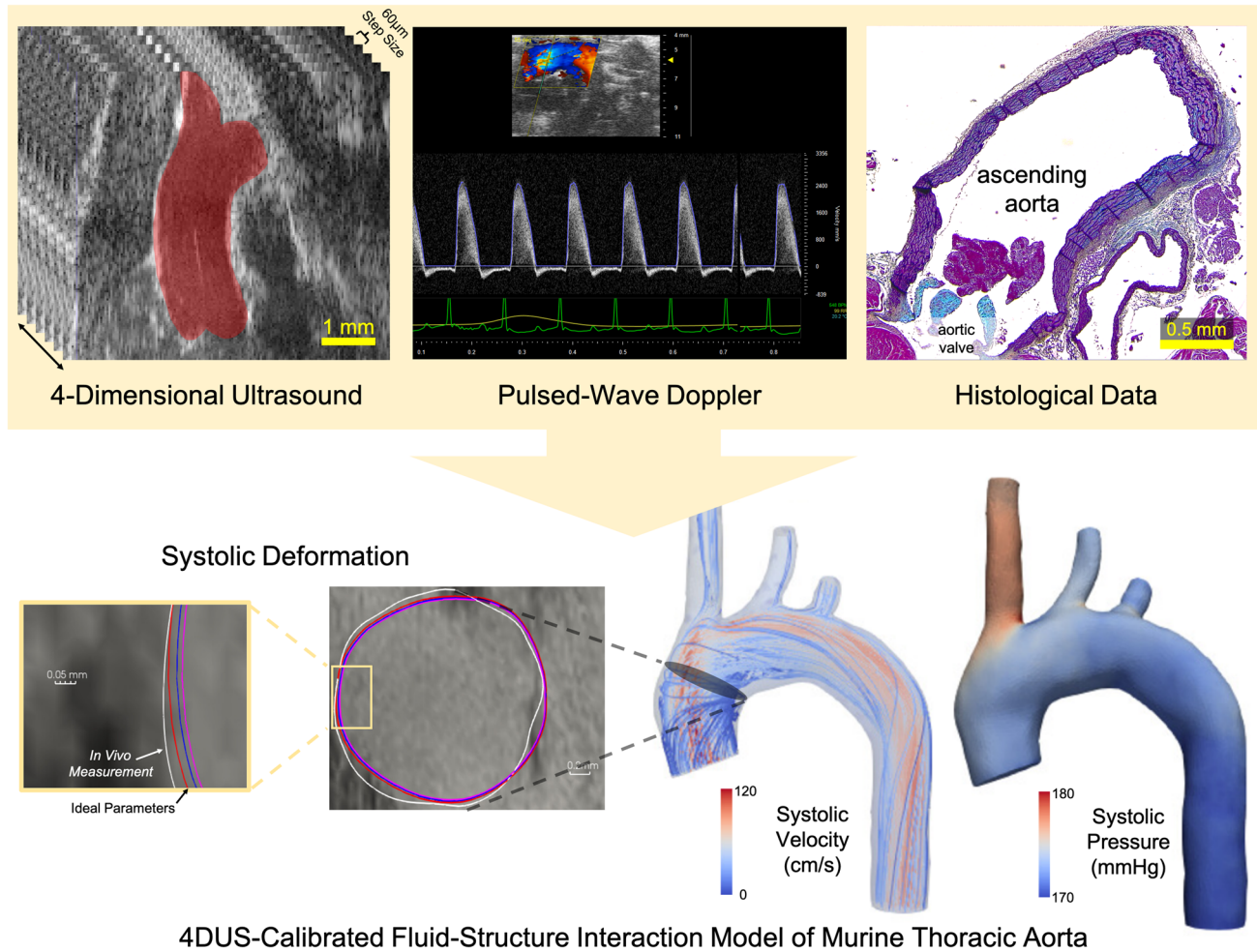hcebull@purdue.edu

Megan C. Madden
madden20@purdue.edu

Ivan C. Christov
christov@purdue.edu

Vitaliy L. Rayz
vrayz@purdue.edu

[1] School of Mechanical Engineering, Purdue University, 585 Purdue Mall, West Lafayette, IN 47907, USA

[2] Weldon School of Biomedical Engineering, Purdue University, 206 S. Martin Jischke Dr., West Lafayette, IN 47907, USA

Graphical abstract

4-Dimensional Ultrasound   Pulsed-Wave Doppler   Histological Data

Systolic Deformation

4DUS-Calibrated Fluid-Structure Interaction Model of Murine Thoracic Aorta

1 Introduction

The thoracic aorta is a highly pulsatile elastic artery in the body [1, 2]. While computational fluid dynamics (CFD) simulations provide an effective technique for quantifying blood flow patterns and estimating hemodynamic parameters, these models lack important biomechanical information on the arterial wall. Furthermore, previous studies have shown that wall shear stress (WSS), an important hemodynamic metric affecting endothelial cell response, is over-estimated in CFD simulations where the wall is assumed to be rigid [3, 4]. Therefore, fluid–structure interaction (FSI) modeling is needed to accurately capture the mechanics of the aortic wall and the effect of feedback between hemodynamic and tissue mechanical forces on hemodynamic quantities of interest. There remains a critical need for improving computational

modeling of the thoracic aorta, as thoracic aortic aneurysms (TAAs) affect 10 out of 100,000 people [5]. Current intervention methods often focus on the volume and diameter of TAAs, neglecting geometry, vessel motion, and effect of blood flow. Importantly, the biomechanics of wall deformation captured through FSI modeling allows for improved understanding of aneurysmal growth and progression by providing better estimates of WSS and other hemodynamic parameters [6, 7]. Therefore, improved biomechanical prediction capabilities through FSI modeling is crucial, as dissections have been reported in patients with vessel diameters below the typical intervention threshold of 5–6 cm [8, 9].

There are many contributing factors to the complexity of TAAs on both micro- and macroscopic scales [10]. On a cellular level, changing levels of elastin, collagen, and inflammatory cells influence the biomechanics of the vessel

[11, 12]. Further, the heart, spine, and other external tissues affect the vessel movement on a macroscopic level [13, 14], and the geometry of the vessel itself (with the aortic valve, arch, and branching vessels) results in complex flow patterns, even in non-diseased cases [15]. Heterogeneous biomechanics of the thoracic aorta should be accounted for through a robust computational methodology that considers all these influencing factors to improve our understanding of the role of biomechanical forces in TAAs, potentially improving non-invasive diagnoses.

In this respect, the most common assumption regarding the motion of the outer vessel wall made in the cardiovascular FSI simulation literature is imposing a zero traction (or homogeneous Neumann) boundary condition. In reality, arterial vessels are constrained within a complex biological environment and imposing a homogeneous Neumann condition results in artificial and often inaccurate vessel wall motion. Moireau et al. [14] proposed to model this external support from surrounding tissue using a Robin boundary condition. Mathematically, this is expressed via the traction $\boldsymbol{\sigma} \cdot \mathbf{n}$, which is determined by the local deformation $\mathbf{u}$ and velocity $\dot{\mathbf{u}}$. Specifically, the condition imposed on the outer wall $\partial\Omega_{outer}$ is

$$\boldsymbol{\sigma} \cdot \mathbf{n} = -k\mathbf{u} - c\dot{\mathbf{u}} - p_0\mathbf{n} \quad \text{on} \quad \partial\Omega_{outer}, \tag{1}$$

where k is an elastic spring constant, c is a viscous damping coefficient, p_0 is a constant pressure value that can represent the intracranial/intrathoracic pressure, and $\mathbf{n}$ is the local unit normal. This approach, also used by Bäumler et al. [16], essentially models tethering of the outer wall to a fictitious medium that provides support similar to a Kelvin-Voigt viscoelastic material. As seen from Eq. (1), this model is characterized by the phenomenological parameters p_0, k and c, which must be modeled or calibrated.

As explained by Moireau et al. [14], this choice of model to account for tissue support requires the above phenomenological parameters (i.e. p_0, k and c) to be calibrated by matching wall deformation data from simulations to in vivo imaging, instead of prescribing direct wall motion data as a strong Dirichlet boundary condition.

The angiotensin II (AngII)-infused mouse model is a popular murine model to study disease progression of both thoracic and abdominal aortic aneurysms [17]. Animals develop hypertension, causing expansion and stiffening within the thoracic aorta and occasionally dissection in the suprarenal abdominal aorta [18]. Recently, there has been increased interest in computational modeling of small animals because of the ability to collect image data both pre- and post-aneurysm formation, with a view towards augmenting experimental measurements with high-resolution computational data [19]. From the perspective of developing high fidelity computational models, the modeling strategy of using tissue support boundary conditions is highly suitable as such models can be easily customized to simulate a variety of experimental conditions in-silico without having to redo animal experiments. However, for the purposes of conducting such FSI simulation studies of murine models, there are limited reports in the literature on suitable values of the tissue support parameters. In this study, we propose to address this gap by performing a longitudinal computational FSI analysis of murine aortas and calibrating the tissue support parameters via comparison to experimental four-dimensional ultrasound (4DUS) data.

2 Methods

2.1 Animals and aortic expansion

Under the approval of the Purdue Animal Care and Use Committee, male wildtype C57BL/6J mice (23.5 g $\pm$ 1.3; 32 weeks old; n = 5) from The Jackson Laboratory (Bar Harbor, ME) were infused with AngII (MW: 1046.19; Bachem, Torrance, CA) for 28 days via subcutaneous implantation of mini-osmotic pumps in the dorsum of each mouse (ALZET Model 2004; DURECT Corporation, Cupertino, CA) [20]. The pumps systemically delivered AngII dissolved in saline solution (0.9% sodium chloride) at a rate of 1000 ng/kg/min. One of the five mice died before the end of the study due to aortic rupture. The remaining four mice were euthanized 28 days post-implantation with an overdose of carbon dioxide.

2.2 Image acquisition, blood pressure, and histology

We acquired high-resolution ultrasound images (Vevo2100 Imaging System; FUJIFILM VisualSonics Inc., Toronto, Ontario, Canada) at baseline and 28 days post AngII infusion for each mouse (referred to hereafter as "Day 0" and "Day 28" time points respectively). We applied a depilatory cream before imaging to remove hair from the region of interest to minimize image artifacts. To obtain inlet velocities, we collected pulsed-wave Doppler (PWD) waveforms. A custom MATLAB code was then used to quantify the PWD data for the inlet flow boundary conditions [21]. To visualize vessel geometry and wall deformation, we collected 4DUS from individual electrocardiogram-gated kilohertz visualization (EKV) cine images. To acquire the 4DUS scans, we used an automated technique that collected an EKV every 60 μm using a 40 MHz center frequency linear array transducer (MS550D FUJIFILM VisualSonics Inc.; axial resolution = 40 μm; lateral resolution = 90 μm) in a long axis view until the majority of the thoracic aorta and branches off of the arch were captured [22].

At the Day 0 and Day 28 time points, we also collected diastolic and systolic blood pressure data from conscious mice using a tail cuff system (CODA 2 Channel Standard, Kent Scientific, Torrington, CT). The mice were acclimated to the cone restraints and tail cuffs prior to collection. Following the final imaging and blood pressure measurements, we excised and fixed the vessels for a histological analysis using Movat's Pentachrome stain. We used the histological slices to obtain average thickness values incorporated in Day 28 wall properties (see image in Figs. 1b and 2a).
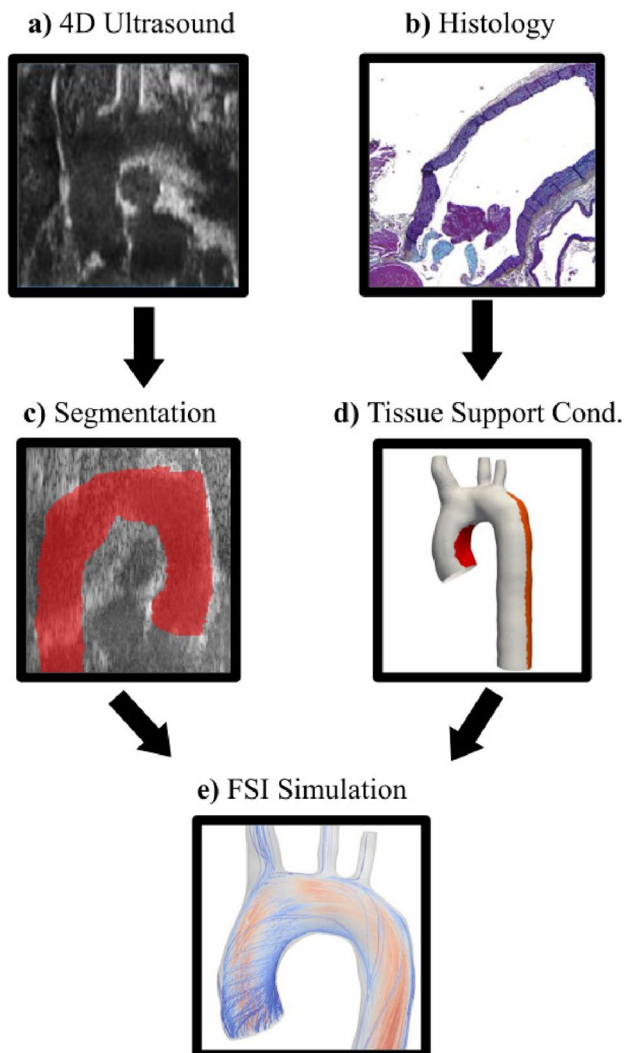

Fig. 1 Proposed modeling pipeline for calibrating tissue support parameters for FSI simulations. Panels **a**–**e** highlight the general steps in this study beginning with **a** acquiring 4DUS data and **b** collecting histological data. Segmentations of the lumen **c** can be extracted to generate the geometry of the flow domain. Meanwhile, histological data provides us geometry of the outer wall (for Day 28) which may then be used to prescribe heterogeneous tissue support parameters (red/white), as in **d**. This is assembled into a physiologically realistic FSI model (**e**) (colour figure online)

2.3 Computational geometries

2.3.1 Fluid domain geometry

We segmented the ultrasound images of flow domain at diastole for one of the mice to use as a representative model. The specific animal case was chosen such that it matched the mean expansion of all four mice in the ascending aorta region ($\approx 70\%$). The geometry included the ascending aorta and portions of the brachiocephalic trunk, left common carotid artery, left subclavian artery, and the descending aorta via 4DUS imaging data acquired at days 0 and 28 as described in Sect. 2.2. We performed the segmentations at end diastole, as well as peak systole to be used for maximum in vivo deformation measurements. We used the open-source three-dimensional (3D) medical image analysis tool ITK-SNAP [23] for segmentation. As the descending aorta was not entirely visible in the image data, we artificially extended the segmentations. We subsequently performed smoothing and cleanup of the geometry in the commercial computer-aided design (CAD) tool Geomagic® Design X to eliminate sharp edges, bumps, and other initial segmentation artifacts.

2.3.2 Solid domain geometry

For the blood flow domain extracted and discussed in Sect. 2.3.1, we estimated the nonuniform arterial wall thickness (the solid computational domain) by solving the Laplace equation over the luminal surface as originally proposed by Bazilevs et al. [24]. Specifically, the thickness $t(\mathbf{x})$ at location $\mathbf{x}$ along the luminal surface (inner wall $\partial\Omega_{inner}$) was found as the solution to:

$$\nabla^2 t(\mathbf{x}) = 0 \quad \text{on} \quad \partial\Omega_{inner}. \tag{2}$$

The domain for the Laplace equation is the inner wall $\partial\Omega_{inner}$, and boundary conditions are prescribed on the sets of curves at the inlets and outlets of the computational geometry.

The thickness values prescribed at the inlet and outlets as boundary conditions are given in Table 1. For the Day 0 time point, thickness values corresponding to 10% of the average vessel inlet/outlet diameter were prescribed,

Table 1 Wall thickness values prescribed at the inlet and outlet locations for each time point

Time point	ATA (mm)	DTA (mm)	BCA (mm)	LCCA (mm)	LSA (mm)
Day 0	0.14	0.12	0.05	0.04	0.03
Day 28	0.15	0.13	0.09	0.07	0.06

ATA ascending thoracic aorta, *DTA* descending thoracic aorta, *BCA* brachiocephalic artery, *LCCA* left common carotid artery, *LSA* left subclavian artery

Fig. 2 Previous literature [25] and histology **a** were used to determine vessel wall thickness at days 0 and 28 respectively. **b** Shows the solid (transparent red) and fluid (blue) segmented domains of the Day 28 model over a static slice of the corresponding 4D ultrasound image. **c**, **e** Show the pulsed-wave Doppler at Day 0 and Day 28 that was used to inform the inlet boundary condition in panel **d**. The Windkessel RCR model used at the outlets, along with heterogeneous (red and white regions) external tissue support (applied to simulate in vivo conditions) on the Day 0 outer wall geometry, are shown in **d** (colour figure online)
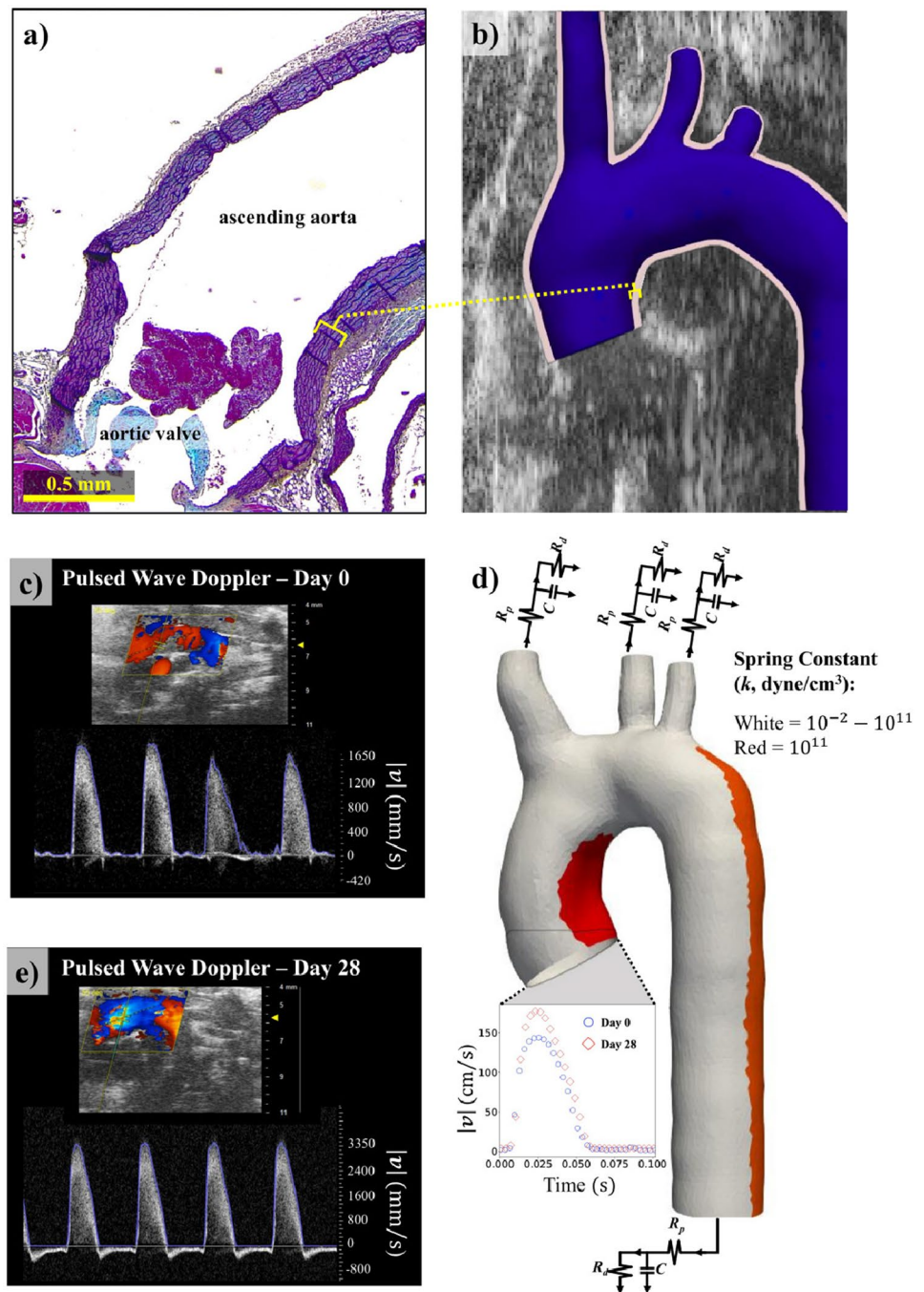
following Hsu and Bazilevs [25]. For the Day 28 time point, we obtained *ex vivo* histology measurements from all four mice at the respective inflow and outflow branches, and we prescribed averaged vessel wall thickness values from these measurements. An example of the geometries for the flow domain and the solid domain is shown in Fig. 2b.

2.4 Mesh generation

Tetrahedral meshes were created for the fluid and solid domains, enforcing node conformity at the fluid–solid interface. To ensure that the shear stress was computed accurately at the fluid–solid interface, we incorporated local mesh refinement in the fluid mesh up to a constant thickness of

0.06 mm from the fluid–solid interface. A grid independence analysis was performed on the Day 0 geometry to ensure that the computational results were independent of the core and near-wall mesh refinement resolutions (see "Appendix 1" for further details).

3 Solver details and boundary conditions

We performed 3D numerical simulations using the svFSI solver within the open-source cardiovascular modeling tool SimVascular [26, 27]. svFSI implements finite element solvers for both the flow and the structural problem. Specifically, an arbitrary Lagrangian–Eulerian (ALE) approach is employed for the FSI coupling, the details of which may be found in [16, 28]. The pertinent governing equations are presented below and further details on the numerical schemes and implementation may be found in [29–31].

3.1 Flow domain

Blood was modeled as a Newtonian fluid with constant density ρ_f and viscosity μ_f, the values of which were obtained from literature data [32] (see Table 2). These values were assumed to be the same for both the Day 0 and 28 time points. The incompressible Navier–Stokes equations were solved in the fluid domain. In the ALE formulation, they are written as:

$$\rho_f \left[\dot{\mathbf{v}} + (\mathbf{v} - \hat{\mathbf{v}}) \cdot \nabla \mathbf{v} \right] = -\nabla p + \mu_f \nabla^2 \mathbf{v}, \tag{3a}$$

$$\nabla \cdot \mathbf{v} = 0. \tag{3b}$$

Here $\hat{\mathbf{v}}$ is the grid velocity of the fluid domain, $\dot{\mathbf{v}}$ is the ALE time derivative of the fluid velocity $\mathbf{v}$, p is the hydrodynamic pressure, and ∇ is the Eulerian gradient operator.

3.2 Structural domain

The arterial wall was modeled as a nearly incompressible isotropic hyperelastic material. A large deformation formulation was used, wherein a mapping between the coordinates in the current configuration $\mathbf{x}$ and the coordinates in the reference configuration $\mathbf{X}$ is obtained. Deformation is then defined as $\mathbf{u} = \mathbf{x} - \mathbf{X}$. The governing equation for the structural problem (neglecting external forces such as gravity), as written in Lagrangian frame, becomes:

$$\rho_s \ddot{\mathbf{u}} + \nabla_{\mathbf{X}} \cdot \left(\mathbf{F} \mathbf{S} \right) = \mathbf{0}. \tag{4}$$

Here, ρ_s is the density of the solid, $\mathbf{u}$ is the displacement, $\ddot{\mathbf{u}}$ is the acceleration, and $\mathbf{F}$ is the deformation gradient, defined as $\mathbf{F} = \nabla_{\mathbf{X}} \mathbf{x} = \mathbf{I} + \nabla_{\mathbf{X}} \mathbf{u}$, where $\nabla_{\mathbf{X}}$ is the gradient with respect to the reference configuration coordinates, and $\mathbf{I}$ is the identity tensor.

The second Piola-Kirchhoff stress tensor $\mathbf{S}$ is determined from the hyperelastic constitutive relation proposed in [33]:

$$\mathbf{S} = 2\frac{\partial \psi}{\partial \mathbf{C}} = \mu_s J^{-2/3} \left(\mathbf{I} - \frac{1}{3} \operatorname{tr} \mathbf{C} \mathbf{C}^{-1} \right) + \frac{1}{2}\kappa \left(J^2 - 1 \right) \mathbf{C}^{-1}, \tag{5a}$$

$$\psi(\mathbf{C}, J) = \frac{1}{2}\mu_s \left(J^{-2/3} \operatorname{tr} \mathbf{C} - 3 \right) + \frac{1}{2}\kappa \left[\frac{1}{2}(J^2 - 1) - \ln J \right]. \tag{5b}$$

Here ψ is the strain-energy density function, $J = \det \mathbf{F}$ is the Jacobian, and $\mathbf{C} = \mathbf{F}^\mathsf{T} \mathbf{F}$ is the right Cauchy–Green deformation tensor. The material parameters μ_s and κ are the shear and bulk moduli of the solid, respectively, which can be expressed in terms of the Young's modulus of elasticity E and the Poisson ratio ν as:

$$\mu_s = \frac{E}{2(1 + \nu)}, \tag{6a}$$

$$\kappa = \frac{E}{3(1 - 2\nu)}. \tag{6b}$$

We assumed different values for E at the Day 0 and 28 time points to account for arterial stiffening due to AngII infusion [34]. These were estimated based on measurements from Bellini et al. [35] (see "Appendix 22" for additional details). Table 2 lists the values of the solid material properties used in the FSI simulations.

3.3 Arterial pre-stress

As pointed out in several previous studies [36–39], the vascular geometry obtained from imaging data is not stress-free.

Table 2 Values of the fluid and solid material properties used for simulations

Property	Day 0	Day 28
Blood density ρ_f	1.06 g/cm^3	1.06 g/cm^3
Blood viscosity μ_f	4 cP	4 cP
Arterial wall density ρ_s	1.0 g/cm^3	1.0 g/cm^3
Arterial wall Young's modulus E	3.11×10^6 dyne/cm^2	3.30×10^6 dyne/cm^2
Arterial wall Poisson ratio ν	0.499	0.499

Rather, it is under continuous mechanical loading due to the incoming fluid flow. Therefore, accounting for the initial loading state of the geometry extracted from imaging data is necessary to obtain accurate vessel wall deformations. In this analysis, we used the methodology proposed by Hsu and Bazilevs [25]. Specifically, the second Piola-Kirchhoff stress tensor $\mathbf{S}$ in Eq. (4) is replaced with the augmented one $\mathbf{S} + \mathbf{S}_0$, where $\mathbf{S}_0$ is an additional pre-stress tensor such that $\mathbf{S}_0$ is in equilibrium with the incoming fluid flow's tractions at diastole.

In this study, the flow traction data were obtained from separate pulsatile rigid-walled flow simulations. Using these simulations as an input, the pre-stress tensor $\mathbf{S}_0$ was estimated for both the Day 0 and Day 28 geometries and prescribed as an initial loading state in subsequent FSI simulations. Additional details on the implementation of the pre-stress estimation methodology in svFSI can be found in [16].

3.4 Fluid domain boundary conditions

To determine the spatial velocity profile at the inlet, the Womersley number,

$$\mathrm{Wo} = R\sqrt{\frac{2\pi f \rho_{\mathrm{f}}}{\mu_{\mathrm{f}}}}, \tag{7}$$

was calculated. Here, R is the vessel radius, f is the cardiac frequency (beats per second), while μ_{f} and ρ_{f} are the dynamic viscosity and density of blood, respectively, as before. The values for Day 0 and Day 28 time points were found to be 2.7 and 2.9, respectively. Since both values were close to $\mathrm{Wo} = 2$, a parabolic flow profile was implemented over the cross-section.

The temporal area-averaged inlet velocity profiles over a single cardiac cycle were acquired at Days 0 and 28 time points for each mouse using PWD measurements. Based on these measurements, we estimated an averaged temporal inlet velocity for our representative Day 0 and Day 28 cases by averaging the velocity values over all four mice. Figure 2d shows the temporal velocity profile used in simulations at both time points. This velocity profile was multiplied by the cross-sectional area at the inlet to obtain the inlet flow rate profile, which was imposed as a parabolic, periodic inlet flow rate boundary condition.

To account for the effect of the downstream vasculature, a three-element Windkessel RCR boundary condition was imposed at each of the outlets [40], as shown in Fig. 2d. An initial estimate of the total arterial resistance R_{total}^0 and capacitance C_{total}^0 was obtained as:

$$R_{\mathrm{total}}^0 = \frac{\tilde{P} - P_0}{\tilde{Q}}, \tag{8a}$$

$$C_{\mathrm{total}}^0 = \frac{Q_s - Q_d}{P_{\mathrm{s}} - P_{\mathrm{d}}} \Delta t. \tag{8b}$$

Here $\tilde{P}$ and $\tilde{Q}$ are the time-averaged pressure and flow rate, respectively, over a single cardiac cycle. Meanwhile, $P_{\mathrm{s}}, Q_{\mathrm{s}}$ and $P_{\mathrm{d}}, Q_{\mathrm{d}}$ are the systolic and diastolic pressures and flow rates, respectively. P_0 is the distal pressure, and Δt is the time difference between Q_{s} and Q_{d}.

Subsequently, as outlined in [41], we tuned the distal pressure, total resistance, and capacitance in an iterative fashion such that both peak systolic (P_{s}) and pulse ($P_{\mathrm{s}} - P_{\mathrm{d}}$) pressures matched the corresponding measured values within an error margin of 10%. We ran rigid-wall pulsatile flow simulations for six cardiac cycles, and the results from the fourth cardiac cycle were used in the fine-tuning process. We further distributed the resistance across each individual outlet using Murray's law ($m = 3$) [42]:

$$R_{\mathrm{out},\ell} = \frac{\sum_{k=1}^{p} \sqrt{A_k^m}}{\sqrt{A_\ell^m}} \cdot R_{\mathrm{total}}. \tag{9}$$

Here R_{total} is the net downstream resistance, A_ℓ is the cross-sectional area of the ℓth outlet, and p is total the number of outlets. The capacitance of each individual outlet branch is calculated as proposed in [41]:

$$C_{\mathrm{out},\ell} = \frac{R_\ell}{R_{\mathrm{total}}} \cdot C_{\mathrm{total}}. \tag{10}$$

For each outlet branch, the ratio of the distal to proximal resistance was assumed to be 1:9 [16]. Tables 3 and 4 list the animal-averaged systolic and diastolic pressures obtained from tail cuff measurements, along with the values obtained via this fine tuning process for the proximal resistance R_{p}, the distal resistance R_{d}, and the capacitance C at each outlet for the Day 0 and Day 28 time points, respectively. We would like to emphasize that the RCR parameter values

Table 3 RCR parameter values at each outlet and pressures for Day 0

Parameters	DTA	BCA	LCCA	LSA
R_{p} ($\times 10^4$ dyne s/cm^5)	1.3	18.5	29.0	86.6
R_{d} ($\times 10^4$ dyne s/cm^5)	11.5	166.7	260.6	779.0
C ($\times 10^{-7}$ cm^5/dyne)	6.3	0.4	0.3	0.1
P_0 (mmHg)	73.2			
P_{s} (mmHg)	115.7			
P_{d} (mmHg)	83.2			

DTA descending thoracic aorta, *BCA* brachiocephalic artery, *LCCA* left common carotid artery, *LSA* left subclavian artery. R_{p} proximal resistance, R_{d} distal resistance, C capacitance, P_0 distal pressure, P_{s} systolic pressure, P_{d} diastolic pressure

Table 4 RCR parameter values at each outlet and pressures for Day 28

Parameters	DTA	BCA	LCCA	LSA
R_{p} ($\times 10^4$ dyne s/cm^5)	1.3	8.7	22.4	11.2
R_{d} ($\times 10^4$ dyne s/cm^5)	11.7	78.0	201.7	100.7
C ($\times 10^{-7}$ cm^5/dyne)	3.8	0.58	0.22	0.45
P_0 (mmHg)	111.4			
P_{s} (mmHg)	164.5			
P_{d} (mmHg)	121.4			

DTA descending thoracic aorta, *BCA* brachiocephalic artery, *LCCA* left common carotid artery, *LSA* left subclavian artery, R_{p} proximal resistance, R_{d} distal resistance C capacitance, P_0 distal pressure, P_{s} systolic pressure, P_{d} diastolic pressure

reported in Tables 3 and 4 are not physiologically realistic but prescribed to ensure that inlet diastolic and pulse pressures are within a 10% margin of corresponding values from cuff measurements.

3.5 Structural boundary conditions

On the natural boundary (i.e. the outer wall), the Robin boundary condition, previously introduced in Eq. (1), was prescribed. Following the work in [16], Eq. 1 was simplified to reduce the number of parameters to be tuned by setting the damping coefficient c and the constant pressure p_0 to 0. Furthermore, a heterogeneous value was prescribed for the spring constant k [14]. Specifically, the outer surface of the arterial wall was divided into three regions to model contact with the spine and pulmonary artery regions (see, e.g., red regions in Fig. 2d) at both the Day 0 and Day 28 time points. Based on observations of wall motion in the 4DUS imaging data, we estimated that the 2D Green-Lagrange strain of the pulmonary artery at the location under the aortic arch did not decrease (3.1% ± 1.1 increase) at Day 28 as we observed in the thoracic aorta (22.5% ± 1.1 decrease), despite expansion of the thoracic aorta from Day 0 to 28 (18.9% increase in diameter). Therefore, both contact areas were simulated by imposing a high stiffness value ($k = 10^9$ dyne/cm^3) to account for this strong tethering. This value was kept constant across all the FSI simulations at Day 0 and 28. A spatially uniform stiffness value, which was progressively varied across different simulations (see Sect. 3.6), was imposed on the remainder of the outer wall, hereafter referred to as the "outer wall with variable tissue support" (see, e.g., white region in Fig. 2d).

For the solid caps at each flow outlet, a homogeneous Dirichlet boundary condition, $\mathbf{u} = \mathbf{0}$, was imposed. This was found to be consistent with imaging data, which showed the outflow branches at the corresponding locations undergoing minimal displacement. Conversely, the artificial boundary ring at the inlet is influenced by heart motion. This effect

was modeled via a Robin boundary condition with the traction prescribed:

$$\boldsymbol{\sigma} \cdot \mathbf{n} = -k(\mathbf{u} \cdot \mathbf{n})\mathbf{n} - c(\dot{\mathbf{u}} \cdot \mathbf{n})\mathbf{n} - p_0\mathbf{n} \quad \text{on} \quad \partial\Omega_{\mathrm{inlet}}, \quad (11)$$

where k, c, p_0, and $\mathbf{n}$ are as previously defined for Eq. (1). In contrast to the boundary condition on the outer wall, given by Eq. (1), the projection onto the normal direction in Eq. (11) was used to preclude out-of-plane deformations of the inlet ring, further guaranteed by imposing a large value for the spring constant ($k = 10^{17}$ dyne/cm^3) and setting c and p_0 to 0.

3.6 FSI simulation parameters

For each time point (Day 0 and Day 28), we ran 3D pulsatile FSI simulations for four cardiac cycles. The inlet Reynolds number at peak systole for an intermediate value of tissue support spring parameter ($k = 10^6$ dyne/cm^3) was estimated to be 358 for the Day 0 time point and 522 for the Day 28 time point. For the Day 0 case, we considered k values from 10^{-2} to 10^{11} dyne/cm^3 (end points included) for the outer wall with variable tissue support (see Sect. 3.5). An additional simulation was run without any external tissue support—in this case, prescribing a homogeneous Neumann condition ($k = 0$) on the outer wall with variable tissue support (white region in Fig. 2d). In total, 15 simulations were performed for Day 0.

Each simulation took approximately 6 h of CPU time to complete all four cardiac cycles on 120 cores of a single compute node, which consisted of two 64-core AMD Epyc 7662 "Rome" processors (Bell Community Cluster, Rosen Center for Advanced Computing, Purdue University, West Lafayette). After determining suitable tissue support parameter values for the Day 0 time point, a subset of the above tissue support parameter range (10^3 to 10^8 dyne/cm^3) was tested for Day 28.

In the results shown below, we verified that periodicity was achieved after the second cardiac cycle and reported data extracted from the last (fourth) cardiac cycle.

4 Results and discussion

4.1 FSI simulations

We present here a comparison of various flow and structural metrics extracted from our FSI simulations at Days 0 and 28. As mentioned in Sect. 3.6, the pulmonary artery and spine tissue support values are fixed while the value prescribed on the remainder of the outer wall is varied. Figure 3 shows the pressure contours, wall shear stress (WSS) magnitude contours and wall deformation contours

Fig. 3 Pressure, WSS, and deformation from pulsatile 3D FSI simulations at peak systole for Day 0. In each row, the left-most image shows the location at which the quantity (i.e. pressure, WSS, or deformation) was computed and the right-most image shows the simulation with the highest tissue support value $k = 10^{11}$ dyne/cm^3 on the outer wall with variable tissue support. The three middle columns show simulation results at the lowest tissue support, $k = 0$ and two intermediate k values, $k = 10^6$ dyne/cm^3 and $k = 10^7$ dyne/cm^3. Overall, minimal differences were observed for pressure between models with and without homogeneous external tissue support while WSS and deformation changed appreciably
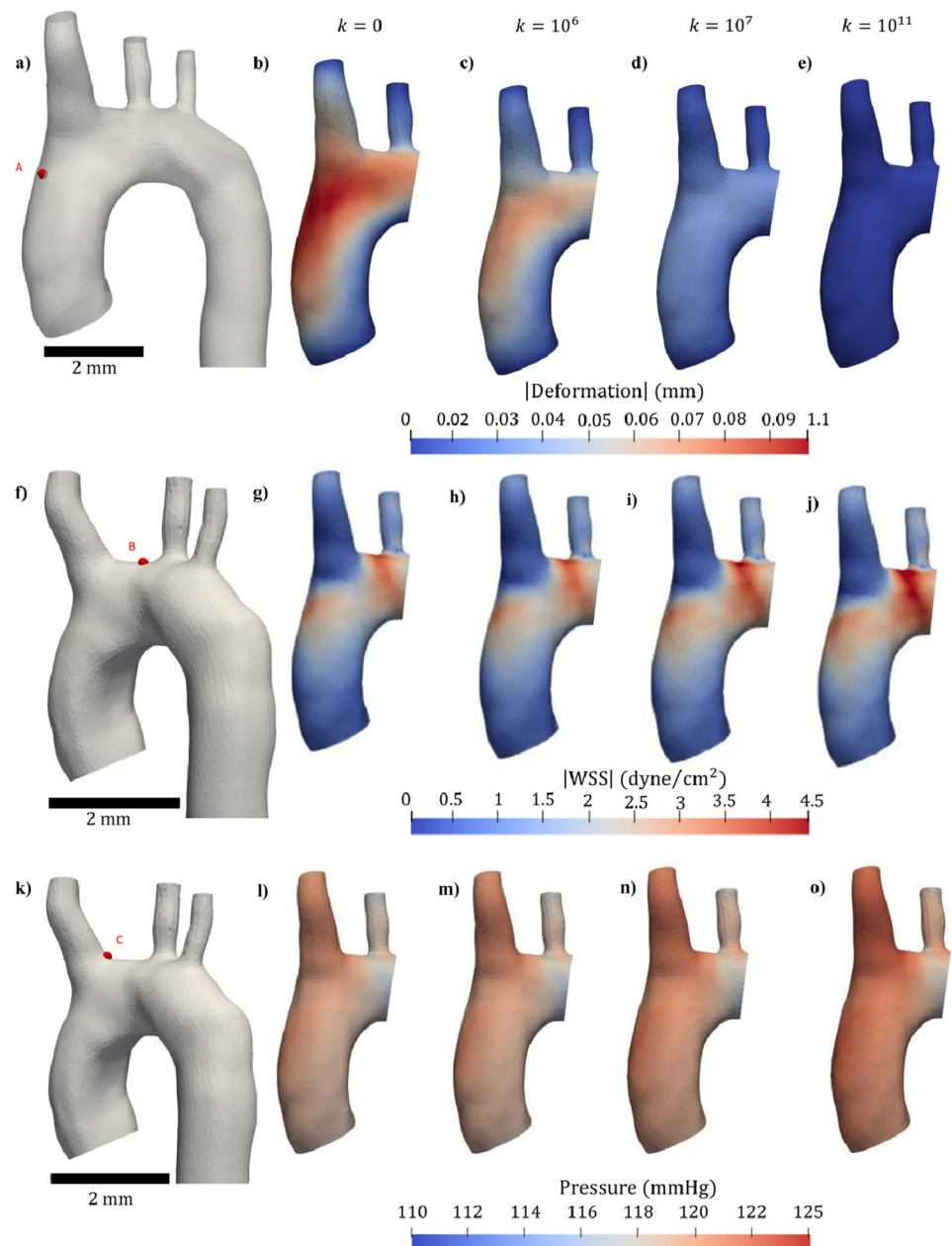
for the largest ($k = 10^{11}$ dyne/cm^3), smallest ($k = 0$) and two intermediate ($k = 10^7$ and 10^8 dyne/cm^3) tissue support values at Day 0. To enable better quantitative comparison, the percentage change (with respect to the least tissue support) in pressure, wall shear stress, and arterial deformation across changing tissue support spring parameter values are listed in Table 5. The comparison is made at three separate points (as shown in Fig. 3a, f, k): Point A, corresponding to the highest spatial peak systolic pressure, Point B, corresponding to the highest spatial peak systolic WSS magnitude and Point C, corresponding to the highest spatial peak deformation magnitude. Point C

is located on the ascending aorta, whereas points A and B are located on the aortic arch. Pressure was found to be minimally affected ($< 2\%$ change from lowest to highest tissue support value) by changes in the value of k. However, an appreciable increase ($\approx 13\%$) in WSS is observable near the aortic arch from $k = 0$ to $k = 10^{11}$ dyne/cm^3. The largest observable change was naturally found to be in the displacement field, with the largest tissue support case being equivalent to assuming a rigid arterial wall.

Large elastic arteries close to the heart undergo non-trivial deformation and translation [14]. Therefore, to determine the goodness of fit between the simulation and imaging data, we extracted cross-sections at three different

Table 5 Percentage change in hemodynamic and structural metrics across varying tissue support spring parameter at Day 0

Quantity	Point	$k = 10^6$	$k = 10^7$	$k = 10^{11}$
Deformation magnitude (%)	A	29.63	68.52	99.95
	B	29.03	69.35	99.92
	C	29.09	73.64	99.97
WSS magnitude (%)	A	3.58	4.25	1.12
	B	1.85	7.88	13.85
	C	2.17	3.89	3.98
Pressure (%)	A	0.15	0.73	1.77
	B	0.16	0.74	1.32
	C	0.12	0.62	1.17

Values of k listed are in dyne/cm^3

WSS wall shear stress

locations within our region of interest (ascending aorta) at peak systole and compared them with corresponding cross-sections from 4DUS imaging data. This comparison was performed for both time points (Day 0 and Day 28). Figure 4 shows the comparison for one of the cross-sections at each time point.

For the Day 0 case, it was observed that except for a small range of values of k, the cross-section profiles coincided with either the highest or lowest tissue support curves. Furthermore, the match between the cross-section from segmentations and the cross-sections from simulations varied with location. For example, in the zoomed-in view of the cross-sections, shown in Fig. 4f, the white curve matches better with the cyan curve ($k = 10^6$ dyne/cm^3) towards the anterior end and the maroon curve ($k = 10^7$ dyne/cm^3) towards the posterior end. This indicated that a qualitative visual comparison would be inadequate to determine a suitable value or range of values which provide the best fit for the 4DUS data. Therefore, we evaluated two quantitative metrics: the effective diameter and the non-overlapping cross-sectional area at all three cross-sections within the region of the ascending aorta at peak systole. The effective diameter, indicative of arterial expansion, was computed as:

$$d_{\text{effective}} = 2\sqrt{\frac{A_{\text{CS}}}{\pi}},$$ (12)

where A_{CS} is the corresponding cross-sectional area. From Eq. (12), it can be seen that a close match between the effective diameter of the simulation cross-sections and ground truth (from imaging) would ensure a choice of the tissue support parameter k which accurately captures vessel expansions/contractions. The non-overlapping area A_{NO} between the cross-sections from segmentation and simulations at a given location was computed as:

$$A_{\text{NO}} = A_{\text{seg}\cup\text{sim}} - A_{\text{seg}\cap\text{sim}}$$
$$= A_{\text{seg}} + A_{\text{sim}} - 2 \cdot A_{\text{seg}\cap\text{sim}}.$$ (13)

Here, A_{seg} is the cross-sectional area obtained from the systolic 4DUS segmentation, A_{sim} is the cross-sectional area at the same location computed from simulations at peak systole for a particular value of tissue support k. Meanwhile, $A_{\text{seg}\cup\text{sim}}$ and $A_{\text{seg}\cap\text{sim}}$ are the areas of the union and intersection of these two cross-sections respectively. Based on the definition, the non-overlapping area is indicative of how closely the simulation results capture not only the arterial expansions/contractions but also vessel translation. Figure 5 shows the variation of the effective diameter and non-overlapping area for different values of tissue support k. For data on the other two cross-sections, we refer the reader to "Appendix 3".

For the Day 0 time point, the variations in effective diameter and non-overlapping area are observed in a narrow range of k values. This was consistent with observations from Fig. 4, where cross-section profiles from simulations were found to be coincident with the highest or lowest tissue support curves except for a small range of $k \in [10^6, 10^7]$ dyne/cm^3. A crossover between the segmentation curve and the simulation points was observed between $k = 10^6$ and $k = 10^7$ dyne/cm^3 (see Fig. 5c). Furthermore, the non-overlapping area corresponding to this range of k values is also the least amongst all simulated cases with varying tissue support parameter, as seen from the plot in Fig. 5e. Based on this data obtained for the Day 0 time point, the range of suitable values of k was chosen to be $[10^6, 10^7]$ dyne/cm^3. The effective diameter obtained from segmentations corresponds to this range of k values and the non-overlapping area is also the least amongst all simulated cases with varying tissue support parameter.

For the diseased aorta at Day 28, we observed that the same range of tissue support values (as that determined from the Day 0 time point, i.e. $k \in [10^6, 10^7]$ dyne/cm^3) was still suitable (see Fig. 5d and f). This observation indicates that the tissue support parameter may be kept identical between healthy and diseased states provided that differences in arterial stiffness between the healthy and diseased state have been accounted for. As noted previously, strain in the ascending thoracic aorta substantially decreased while remaining the same in the pulmonary artery suggesting that AngII has a larger effect on the higher pressure in systemic circulation.

4.2 Limitations

The study had several limitations related to image acquisition, computational assumptions, and certain limitations of the svFSI framework. While 4DUS is an accessible option

Fig. 4 Visual comparison of 4DUS and FSI simulation data at peak systole. **a**, **b** Show the locations of the cross-sections being considered at Day 0 and Day 28 respectively. **c**, **d** Show the cross-sections (colored rings) obtained for varying values of tissue support parameter k (in dyne/cm^3) overlaid on the 4DUS image slice at the corresponding cross-section at peak systole. The corresponding segmentation cross-section is shown by the white ring. **e**, **f** represent zoomed-in views of regions on the cross-section (represented by the yellow box in **c**, **d**). The white bar in subpanels (**c**–**f**) corresponds to a scale of 0.2 mm (colour figure online)
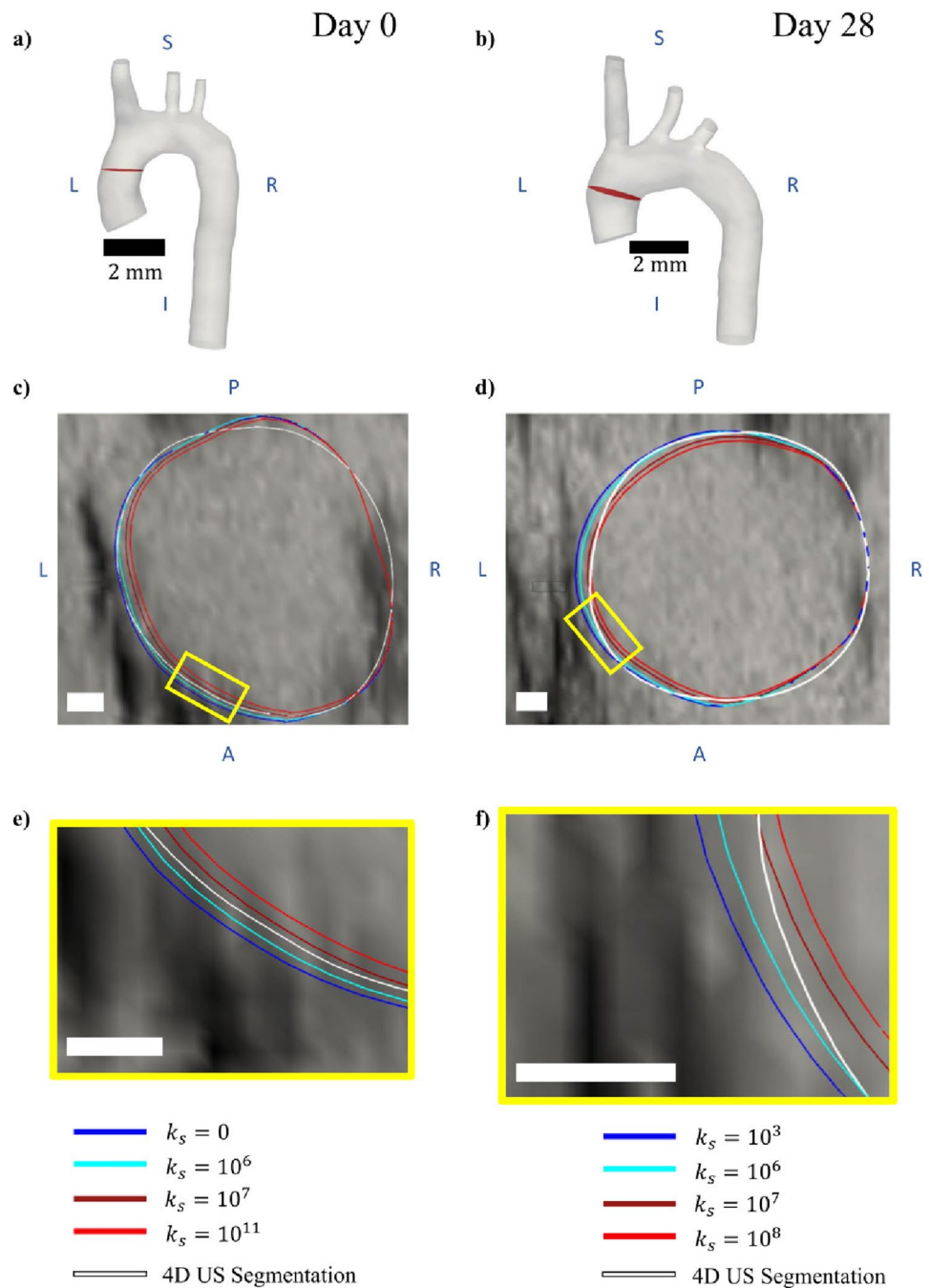
for studies in mice, the clinical translation is currently limited. Petterson et al. [43] have taken a step toward this implementation with a recent study using multi-perspective ultrasound to mechanically characterize the aorta. Until 4DUS becomes more widely available, the presented FSI approach would work with other time-resolved imaging methods such as cardiac-gated computed tomography or magnetic resonance, although these methods typically have much lower temporal resolution.

We also note the limitations when using murine TAA models, as the hemodynamic characteristics are clearly different between mice and humans. Nevertheless, the blood velocities, systemic pressure, and cyclic strain are similar across mammals. Further, we were able to collect multiple time points and tissue for analysis, which allowed us to compare simulation results for Day 0 with our Day 28 simulation using the same external tissue supports. In terms of our simulation approach, the present analysis assumed

Fig. 5 Quantitative metrics comparing segmentations from 4DUS and FSI simulations for different values of k at peak systole. **a, b** Show the location of the cross-section being considered, which is the same as in Fig. 4a, b. Red squares in **c, d** show the plot of effective diameter of the cross-section, obtained from FSI simulations (calculated using Eq. (12)) as a function of tissue support parameter k. The solid red line represents the effective diameter of the same cross-section obtained from segmentations of 4DUS imaging data. **e, f** Show the variation of non-overlapping area at the cross-section, calculated using Eq. (13), as a function of the varying tissue support parameter k (colour figure online)
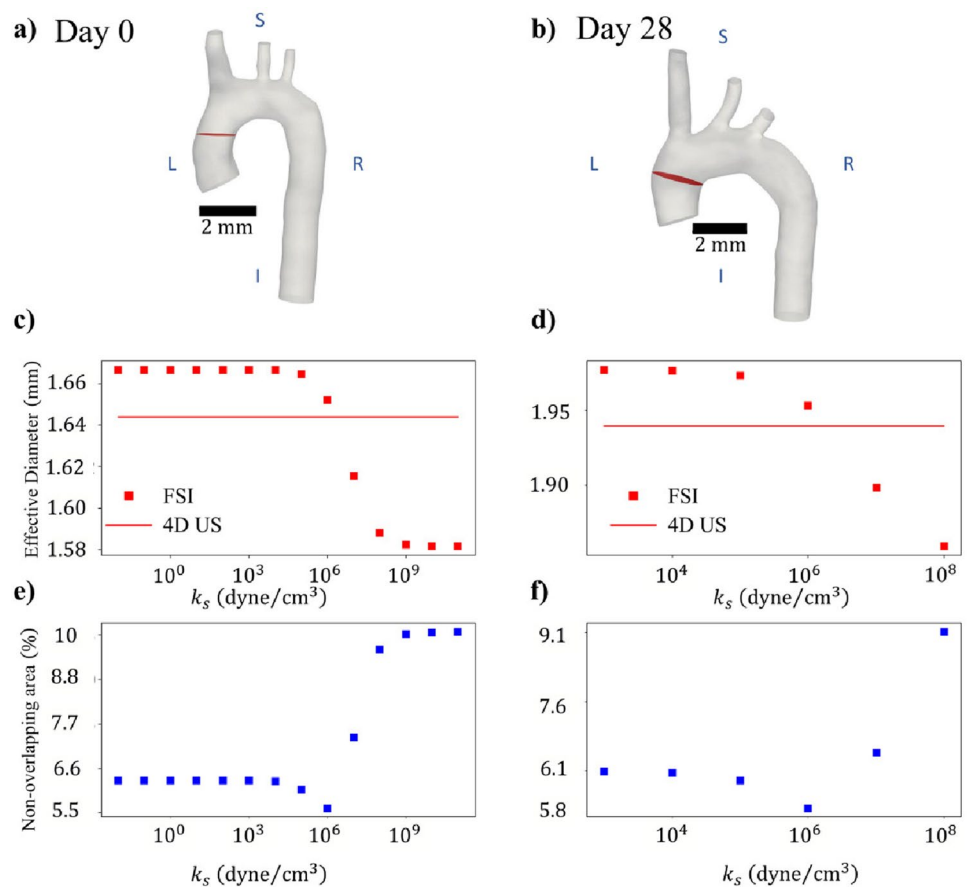
uniform material properties (values of E and v) throughout entire arterial wall region being modeled. Furthermore, an isotropic hyperelastic constitutive model was chosen. In reality, arterial wall properties are not only animal-specific, but also highly anisotropic, as shown in this recent work [44]. However, in the absence of any animal specific measurements on mechanical properties of the aortic wall, a simplifying assumption that the arterial wall material properties were isotropic, constant and could be extracted from available literature data was made in our analysis.

In this analysis, the out-of-plane deformations of the aortic root are neglected owing to limitations of svFSI associated with imposing a parabolic flow inlet profile. In reality, some amount of longitudinal displacement is expected due to the motion of the aortic root. As seen from the study by Moireau et al. [14], as well as a recent computational study of thoracic aortic aneurysms in human subjects [46], this motion is found to be more important in the healthy state as compared to the diseased state. However, allowing for in-plane deformations enables accounting for some if not the entire motion of the aortic root. Future work on developing a more advanced computational framework and better arterial wall characterization techniques is needed to optimize both

animal- and patient-specific material properties and tissue support parameters for FSI simulations.

In the present study, it was sufficient to assume a linear elastic mechanical response of the surrounding biological environment, and the effect of the damping coefficient in the tissue support model was neglected. To provide further support for this approach, we compared simulation results with identical spring constants but different damping coefficients, and we observed that the damping component of the tissue support model does not affect peak systolic vessel wall deformations. In general, it is reasonable to expect that surrounding tissue and the tethering of blood vessels can be represented as viscoelastic supports, characterised by non-zero values of both the spring constant k and the damping coefficient c. Thus, one could expect damping to affect the vessel wall velocity and acceleration profiles. However, tuning the additional damping coefficient would require data on vessel wall velocities, which is unavailable in the present analysis. Therefore, the current model could be extended in the future, incorporating both displacement and velocity data to simultaneously tune k and c.

Except for the spine and pulmonary artery regions, which are rigid contacts, a spatio-temporally uniform value of k

was assumed over the remaining surface of the outer wall. However, as seen in cross-sectional comparisons from Fig. 4, parts of the curve segmented from 4DUS data matched better using different values of the tissue support parameter k. Moreover, the response of the surrounding tissue is generally expected to be anisotropic, non-linear and dependent on the stage in the cardiac cycle. This is particularly important for vessels close to the heart, that can be affected by motion of the lungs during regular respiration. While accounting for these limitations is out of the scope of the present analysis, we demonstrated the effect of incorporating some tissue support parameters and obtained a suitable range for these tissue support parameters. Accounting for heterogeneity in these values (by accurately considering the various types of contacts and supports) would further improve the fidelity of computational models.

Lastly, testing these support parameter estimates on a statistically powerful sample size could help assess the animal-specific robustness.

5 Conclusion

Using 4DUS imaging data, we were able to model both blood flow and vessel wall deformation of the murine thoracic aorta, accounting for the effect of surrounding tissue on the outer wall. We determined a suitable range of tissue support parameter values in the FSI model, $k \in [10^6, 10^7]$ dyne/cm^3, for both non-diseased and hypertensive expanded aortas, such that arterial wall deformations predicted by simulations were in good agreement with 4DUS measurements at peak systole. While it is shown that incorporating at least some tissue support would greatly improve predictions of computational FSI models, additional data on the nature of vessel wall contact is critical for fine-tuning of these values. Overall, this study presented a methodology for incorporating heterogeneous tissue support parameters in FSI simulations to better capture physiologically realistic vessel wall deformation. Further, this study provided estimates (ranges) for the tissue support parameters validated using in vivo imaging data. In future work, the proposed methodology could help improve the clinical assessments of aortic disease.
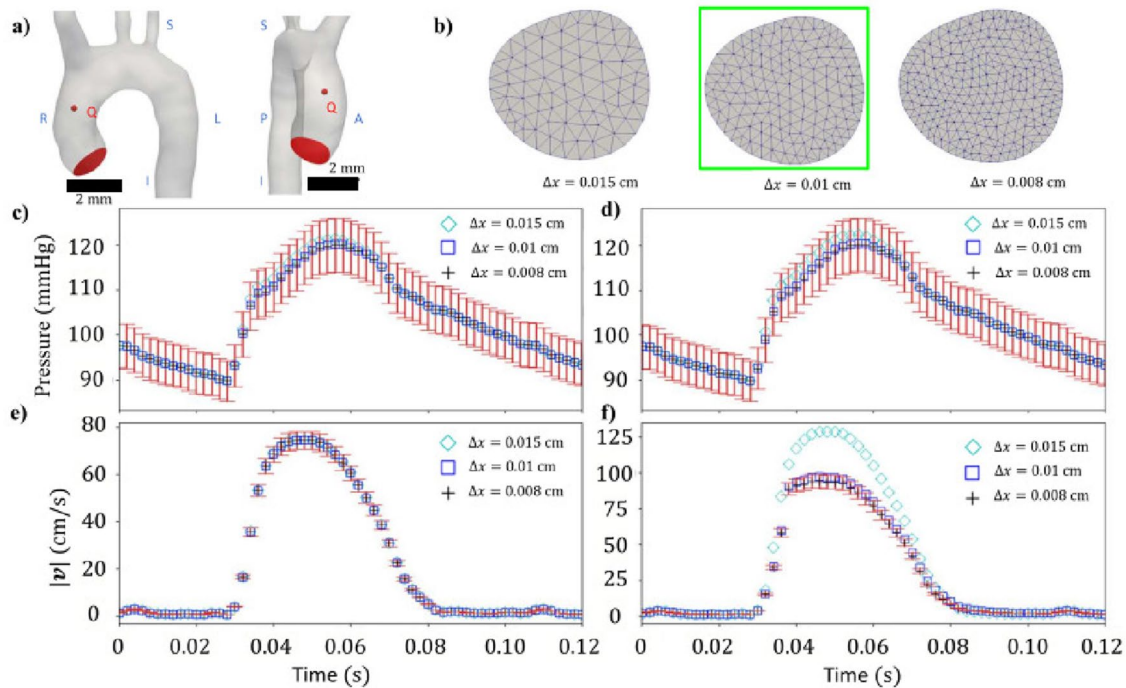

Fig. 6 Pressure and velocity data over a cardiac cycle at the inlet plane (panels **c** and **e**) and at a point (panels **d** and **f**) in the interior of the ascending aorta (shown in **a**) for different mesh resolutions (shown in **b**). The error bars of each plot point show a deviation of 5% from the corresponding value on the finest mesh ($\Delta x = 0.008$ cm). Abbreviations used—|**v**| Velocity magnitude, *R* Right, *L* Left, *A* Anterior, *P* Posterior. Based on the above plots, $\Delta x = 0.01$ cm was chosen as the optimal core mesh resolution

Appendix 1: Grid independence

To ensure that computational quantities reported, such as pressure, velocity and wall shear stress, were independent of the grid resolution of the fluid domain's mesh, a grid sensitivity analysis was performed. The pertinent details for each mesh are shown in Table 6. A two-step approach was used to establish grid independence. First, a core mesh resolution was determined such that pressure and velocity were independent of the core mesh resolution. Second, varying degrees of mesh refinement close to the fluid–solid interface were implemented on top of the chosen core mesh resolution from the previous step, to ensure that the computed wall shear stress was independent of the near-wall mesh refinement resolution. In Fig. 6c–f, the area-averaged and point-wise pressure and velocity magnitude at the inlet plane, as well as at an arbitrary point located in the interior of the ascending region of the aorta (see Fig. 6a) are plotted over a single cardiac cycle.

Based on the plots in Fig. 6c–f, we observed that the pressure and velocity magnitude values computed on both

the coarse and medium grid (i.e. with $\Delta x = 0.015$ cm and $\Delta x = 0.01$ cm) lie within a 5% margin of the values computed on the fine grid. However, in Fig. 6d, the velocity magnitude for the coarse grid ($\Delta x = 0.015$ cm) lies beyond this tolerance margin. Therefore, $\Delta x = 0.01$ cm was determined to be the core mesh resolution of choice.

Next, Fig. 7 shows the x, y, and z components of the WSS (wall shear stress) computed at a point on the surface of the ascending aorta. Here, the core mesh resolution was identical in all cases ($\Delta x = 0.01$ cm). However, close to the fluid–solid interface, different number of layers of mesh refinement (0, 3,

Table 6 Mesh details for grid optimization

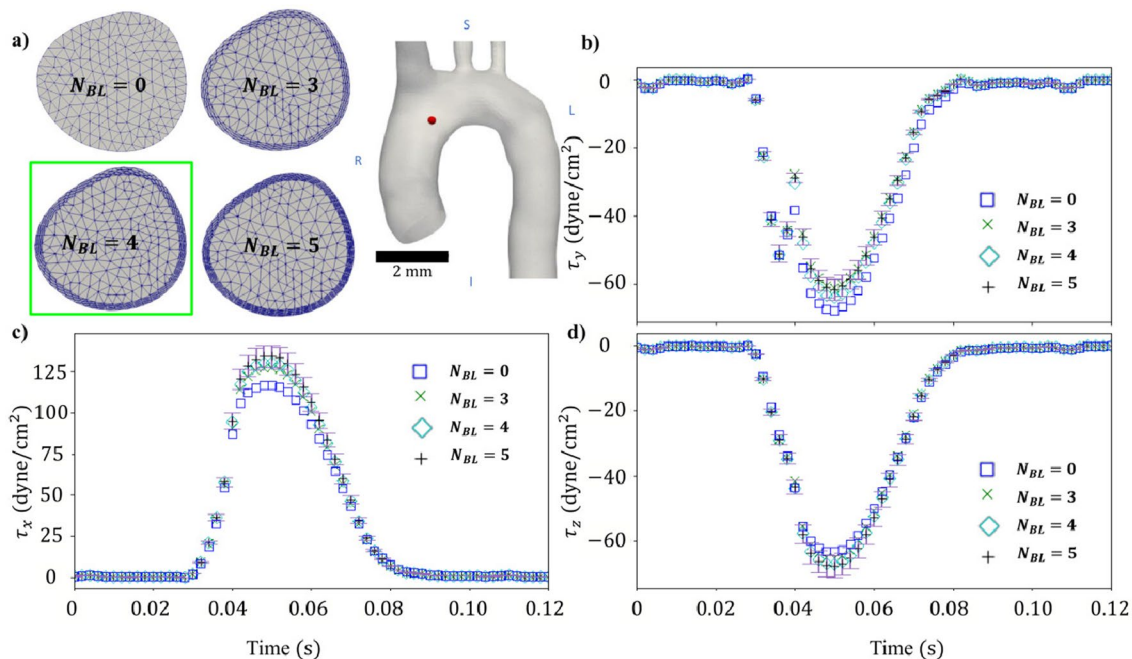| Δx_{core} (cm)	N_{BL}	$N_{elements}$	N_{nodes}	Max. CFL
0.01	0	169,749	32,750	0.4
	3	189,832	36,375	1.04
	4	190,015	36,401	1.05
	5	191,098	36,744	1.01
0.15		53,032	11,078	0.28
0.08		326,791	61,263	0.49

Fig. 7 Components (**b**–**d**) of the WSS over a cardiac cycle at a point on the interior surface of the ascending aorta (shown by a dot in the model geometry in **a**), for different number of boundary layers each. N_{BL} represents the number of layers of boundary layer elements. Here, $N_{BL} = 0$ represents a mesh without boundary layer refinement. The error bars on each plot point show a deviation of 5% from the corresponding value on the mesh with the largest number of boundary layer refinements (i.e. $N_{BL} = 5$). Based on the above plots, the boundary layer mesh resolution corresponding to $N_{BL} = 4$ was chosen as for the FSI simulations. Abbreviations used—*R* Right, *L* Left, *S* Superior, *I* Inferior

Fig. 8 Experimental circumferential stress-stretch-squared data from Bellini et al. [35] along with best fit lines and corresponding best fit equations (with units implied). The Young's modulus (in kPa) was estimated to be three times the fitted slope (colour figure online)
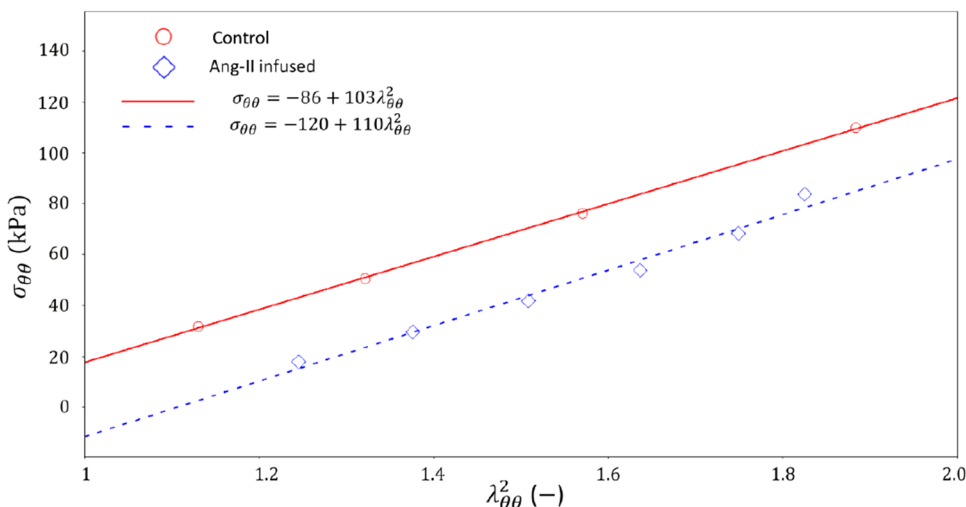
4, and 5) were considered (see Fig. 7a) From Fig. 7b–d, we observed a non-trivial difference ($> 5\%$) between the surface shear stress values computed on meshes with and without mesh refinement. Furthermore, meshes with different levels of mesh refinement ($N_{BL} = 3, 4$, and 5) yield shear stress values within the above tolerance limit with minor differences in the computation time. Therefore, we proceeded with a mesh refinement level of $N_{BL} = 4$, to balance the need for increased resolution with the corresponding computational cost.

A constant time step of $\Delta t = 10^{-5}$ s was used for all cases. Table 6 reports an estimate of the maximum cell-based Courant number computed for each of the meshes used, over a single cardiac cycle. The Courant number was computed as:

$$CFL = \frac{|\mathbf{v}|\Delta t}{\Delta x}, \tag{14}$$

where $|\mathbf{v}|$ is the velocity magnitude at the cell center, Δt is the time step size, and Δx is a length scale computed for each cell as $\Delta x = \mathcal{V}^{1/3}$, where $\mathcal{V}$ is the cell volume.

We observed that, for cases for which the maximum CFL > 1, only a few cells (< 5) outside the region of interest (viz. the ascending aorta) exceeded the threshold. This observation, together with the fact that the time integration scheme implemented in svFSI is an implicit scheme [45], allowed us to use the same time step size of $\Delta t = 10^{-5}$ s for the subsequent FSI simulations as well.

Appendix 2: Material properties

The Young's moduli for the Day 0 and 28 time points were estimated using circumferential stress-stretch data for wildtype C57BL/6J and AngII-infused apolipoprotein E$^{-/-}$ mice, respectively, as reported by Bellini et al. [35]. For a biaxial state of stress of an incompressible neo-Hookean material, the theoretical relationship between circumferential stress $\sigma_{\theta\theta}$ and circumferential stretch ratio $\lambda_{\theta\theta}$ is:

$$\sigma_{\theta\theta} = -p + \frac{E}{3}\lambda_{\theta\theta}^2, \tag{15}$$

where p is the Lagrange multiplier that enforces the incompressibility constraint. Therefore, using the biaxial stress-stretch data reported in [35], the Young's modulus was estimated to be three times the slope of the best fit line to $\sigma_{\theta\theta}$ versus $\lambda_{\theta\theta}$ (see Fig. 8). The values are reported in Table 2.

Appendix 3: Comparison of other cross-sections

This appendix provides plots of the effective diameter and non-overlapping area (see Sect. 4.1) at the other two cross-sections for the Day 0 and Day 28 time points (Figs. 9 and 10). Overall, the observations regarding these cross-sections are consistent with the data obtained for the cross-section reported in Sect. 4.1.
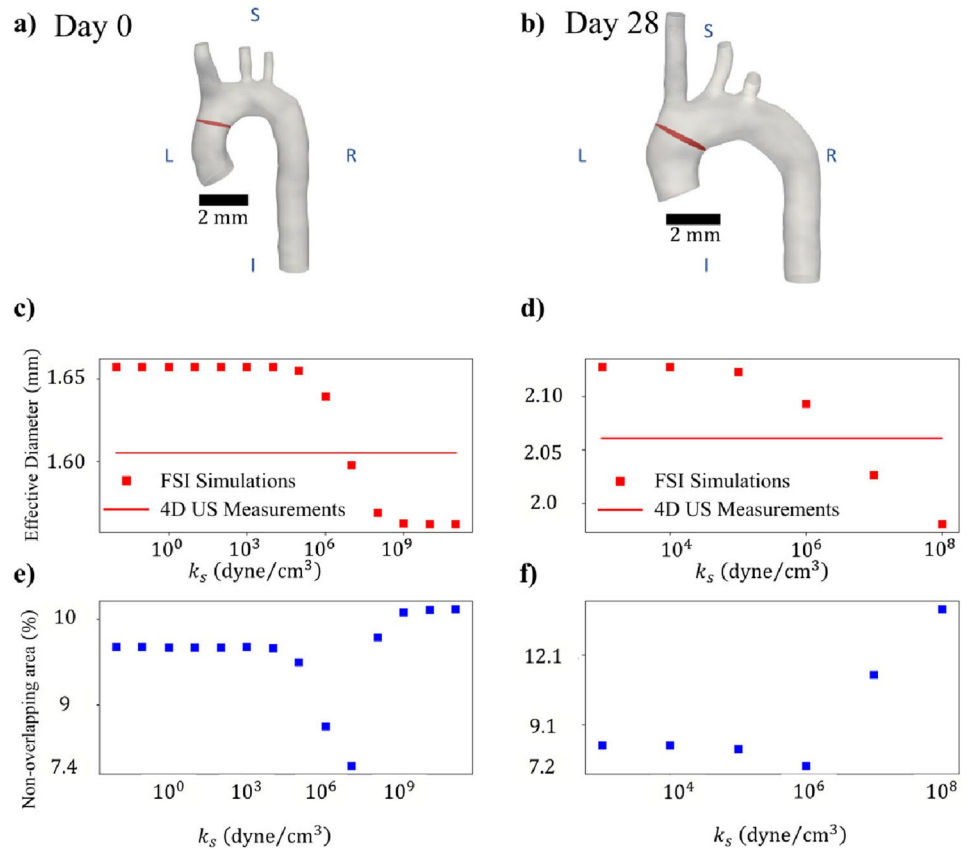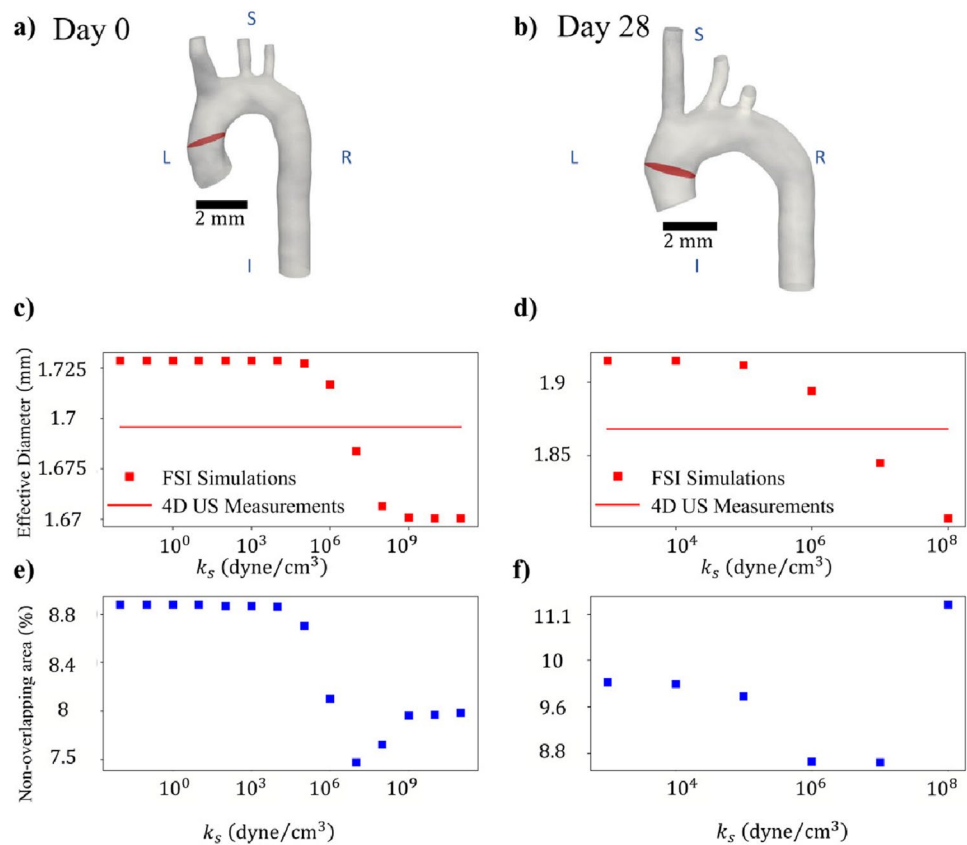
Fig. 9 Quantitative metrics comparing segmentations from 4DUS and FSI simulations for different values of k at peak systole. **a**, **b** Show the location of the cross-section being considered. Red squares in **c**, **d** show the plot of effective diameter of the cross-section, obtained from FSI simulations (calculated using Eq. (12)) as a function of tissue support parameter k. The solid red line represents the effective diameter of the same cross-section obtained from segmentations of 4DUS imaging data. **e**, **f** Show the variation of non-overlapping area at the cross-section, calculated using Eq. (13) as a function of the varying tissue support parameter k (colour figure online)

Fig. 10 Quantitative metrics comparing segmentations from 4DUS and FSI simulations for different values of k at peak systole. **a**, **b** Show the location of the cross-section being considered. Red squares in **c**, **d** show the plot of effective diameter of the cross-section, obtained from FSI simulations (calculated using Eq. (12)) as a function of tissue support parameter k. The solid red line represents the effective diameter of the same cross-section obtained from segmentations of 4DUS imaging data. **e**, **f** Show the variation of non-overlapping area at the cross-section, calculated using Eq. (13) as a function of the varying tissue support parameter k (colour figure online)

Declarations

Conflict of interest Dr. Goergen is a paid consultant and member of the Scientific Advisory Board for FUJIFILM VisualSonics, Inc. None of the authors have a conflict of interest to declare.

References

1. Figueroa CA, Taylor CA, Chiou AJ, Yeh V, Zarins CK (2009) Magnitude and direction of pulsatile displacement forces acting on thoracic aortic endografts. J Endovasc Ther 16(3):350–358. https://doi.org/10.1583/09-2738.1

2. Bracamonte JH, Wilson JS, Soares JS (2020) Assessing patient-specific mechanical properties of aortic wall and peri-aortic structures from *in vivo* DENSE magnetic resonance imaging using an inverse finite element method and elastic foundation boundary conditions. J Biomech Eng 142(12):121011. https://doi.org/10.1115/1.4047721

3. Takizawa K, Bazilevs Y, Tezduyar TE, Long CC, Marsden AL, Schjodt K (2014) ST and ALE-VMS methods for patient-specific cardiovascular fluid mechanics modeling. Math Models Methods Appl Sci 24(12):2437–2486. https://doi.org/10.1142/S0218202514500250

4. Freidoonimehr N, Chin R, Zander A, Arjomandi M (2022) A review on the effect of temporal geometric variations of the coronary arteries on the wall shear stress and pressure drop. J Biomech Eng 144(12):010801. https://doi.org/10.1115/1.4051923

5. Elefteriades JA, Sang A, Kuzmik G, Hornick M (2015) Guilt by association: paradigm for detecting a silent killer (thoracic aortic aneurysm). Open Heart 2(1):e000169. https://doi.org/10.1136/openhrt-2014-000169

6. Campobasso R, Condemi F, Viallon M, Croisille P, Campisi S, Avril S (2018) Evaluation of peak wall stress in an ascending thoracic aortic aneurysm using FSI simulations: effects of aortic stiffness and peripheral resistance. Cardiovasc Eng Technol 9(4):707–722. https://doi.org/10.1007/s13239-018-00385-z

7. Pons R, Guala A, Rodríguez-Palomares JF, Cajas JC, Dux-Santoy L, Teixidó-Tura G, Molins JJ, Vázquez M, Evangelista A, Martorell J (2020) Fluid–structure interaction simulations outperform computational fluid dynamics in the description of thoracic aorta haemodynamics and in the differentiation of progressive dilation in Marfan syndrome patients. R Soc Open Sci 7(2):191752. https://doi.org/10.1098/rsos.191752

8. Booher AM, Eagle KA (2011) Diagnosis and management issues in thoracic aortic aneurysm. Am Heart J 162(1):38–46. https://doi.org/10.1016/j.ahj.2011.04.010

9. Wang Z, Flores N, Lum M, Wisneski AD, Xuan Y, Inman J, Hope MD, Saloner DA, Guccione JM, Ge L, Tseng EE (2021) Wall stress analyses in patients with ≥ 5 cm versus < 5 cm ascending thoracic aortic aneurysm. J Thorac Cardiovasc Surg 162(5):1452–1459. https://doi.org/10.1016/j.jtcvs.2020.02.046

10. Cebull HL, Rayz VL, Goergen CJ (2020) Recent advances in biomechanical characterization of thoracic aortic aneurysms. Front Cardiovas Med 7:75. https://doi.org/10.3389/fcvm.2020.00075

11. Karimi A, Milewicz DM (2016) Structure of the elastin-contractile units in the thoracic aorta and how genes that cause thoracic aortic aneurysms and dissections disrupt this structure. Can J Cardiol 32(1):26–34. https://doi.org/10.1016/j.cjca.2015.11.004

12. Korenczuk CE, Dhume RY, Liao KK, Barocas VH (2019) *Ex vivo* mechanical tests and multiscale computational modeling highlight the importance of intramural shear stress in ascending thoracic aortic aneurysms. J Biomech Eng 141(12):121010. https://doi.org/10.1115/1.4045270

13. Reymond P, Crosetto P, Deparis S, Quarteroni A, Stergiopulos N (2013) Physiological simulation of blood flow in the aorta: comparison of hemodynamic indices as predicted by 3-D FSI, 3-D rigid wall and 1-D models. Med Eng Phys 35(6):784–791. https://doi.org/10.1016/j.medengphy.2012.08.009

14. Moireau P, Xiao N, Astorino M, Figueroa CA, Chapelle D, Taylor CA, Gerbeau J-F (2012) External tissue support and fluid–structure simulation in blood flows. Biomech Model Mechanobiol 11(1–2):1–18. https://doi.org/10.1007/s10237-011-0289-z

15. Markl M, Draney MT, Hope MD, Levin JM, Chan FP, Alley MT, Pelc NJ, Herfkens RJ (2004) Time-resolved 3-dimensional velocity mapping in the thoracic aorta. J Comput Assist Tomogr 28(4):459–468. https://doi.org/10.1097/00004728-200407000-00005

16. Bäumler K, Vedula V, Sailer AM, Seo J, Chiu P, Mistelbauer G, Chan FP, Fischbein MP, Marsden AL, Fleischmann D (2020) Fluid-structure interaction simulations of patient-specific aortic dissection. Biomech Model Mechanobiol 19(5):1607–1628. https://doi.org/10.1007/s10237-020-01294-8

17. Daugherty A, Rateri DL, Charo IF, Owens AP, Howatt DA, Cassis LA (2010) Angiotensin II infusion promotes ascending aortic aneurysms: attenuation by CCR2 deficiency in apoE–/– mice. Clin Sci 118(11):681–689. https://doi.org/10.1042/CS20090372

18. Daugherty A, Manning MW, Cassis LA (2000) Angiotensin II promotes atherosclerotic lesions and aneurysms in apolipoprotein *E*-deficient mice. J Clin Investig 105(11):1605–1612. https://doi.org/10.1172/JCI7818

19. Acuna A, Berman AG, Damen FW, Meyers BA, Adelsperger AR, Bayer KC, Brindise MC, Bungart B, Kiel AM, Morrison RA, Muskat JC, Wasilczuk KM, Wen Y, Zhang J, Zito P, Goergen CJ (2018) Computational fluid dynamics of vascular disease in animal models. J Biomech Eng 140(8):080801. https://doi.org/10.1115/1.4039678

20. Adelsperger AR, Phillips EH, Ibriga HS, Craig BA, Green LA, Murphy MP, Goergen CJ (2018) Development and growth trends in angiotensin II-induced murine dissecting abdominal aortic aneurysms. Physiol Rep 6(8):e13668. https://doi.org/10.14814/phy2.13668

21. Phillips EH, Di Achille P, Bersi MR, Humphrey JD, Goergen CJ (2017) Multi-modality imaging enables detailed hemodynamic simulations in dissecting aneurysms in mice. IEEE Trans Med Imaging 36(6):1297–1305. https://doi.org/10.1109/TMI.2017.2664799

22. Damen FW, Berman AG, Soepriatna AH, Ellis JM, Buttars SD, Aasa KL, Goergen CJ (2017) High-frequency 4-dimensional ultrasound (4DUS): a reliable method for assessing murine cardiac function. Tomography 3(4):180–187. https://doi.org/10.18383/j.tom.2017.00016

23. Yushkevich PA, Piven J, Hazlett HC, Smith RG, Ho S, Gee JC, Gerig G (2006) User-guided 3D active contour segmentation of anatomical structures: significantly improved efficiency and

reliability. Neuroimage 31(3):1116–1128. https://doi.org/10.1016/j.neuroimage.2006.01.015

24. Bazilevs Y, Hsu M-C, Benson DJ, Sankaran S, Marsden AL (2009) Computational fluid–structure interaction: methods and application to a total cavopulmonary connection. Comput Mech 45(1):77–89. https://doi.org/10.1007/s00466-009-0419-y

25. Hsu M-C, Bazilevs Y (2011) Blood vessel tissue prestress modeling for vascular fluid–structure interaction simulation. Finite Elem Anal Des 47(6):593–599. https://doi.org/10.1016/j.finel.2010.12.015

26. Updegrove A, Wilson NM, Merkow J, Lan H, Marsden AL, Shadden SC (2017) SimVascular: an open source pipeline for cardiovascular simulation. Ann Biomed Eng 45(3):525–541. https://doi.org/10.1007/s10439-016-1762-8

27. Lan H, Updegrove A, Wilson NM, Maher GD, Shadden SC, Marsden AL (2018) A re-engineered software interface and workflow for the open-source simvascular cardiovascular modeling package. J Biomech Eng 140(2):024501. https://doi.org/10.1115/1.4038751

28. Vedula V, Lee J, Xu H, Kuo C-CJ, Hsiai TK, Marsden AL (2017) A method to quantify mechanobiologic forces during zebrafish cardiac development using 4-D light sheet imaging and computational modeling. PLoS Comput Biol 13(10):1005828. https://doi.org/10.1371/journal.pcbi.1005828

29. Bazilevs Y, Calo VM, Hughes TJR, Zhang Y (2008) Isogeometric fluid–structure interaction: theory, algorithms, and computations. Comput Mech 43(1):3–37. https://doi.org/10.1007/s00466-008-0315-x

30. Esmaily-Moghadam M, Bazilevs Y, Marsden AL (2013) A new preconditioning technique for implicitly coupled multidomain simulations with applications to hemodynamics. Comput Mech 52(5):1141–1152. https://doi.org/10.1007/s00466-013-0868-1

31. Taylor CA, Hughes TJR, Zarins CK (1998) Finite element modeling of blood flow in arteries. Comput Methods Appl Mech Eng 158(1–2):155–196. https://doi.org/10.1016/S0045-7825(98)80008-X

32. Soudah E, Ng EYK, Loong TH, Bordone M, Pua U, Narayanan S (2013) CFD modelling of abdominal aortic aneurysm on hemodynamic loads using a realistic geometry with CT. Comput Math Methods Med 2013:1–9. https://doi.org/10.1155/2013/472564

33. Simo JC, Hughes TJR (1998) Computational inelasticity. Interdisciplinary applied mathematics, vol 7. Springer, New York. https://doi.org/10.1007/b98904

34. Weiss D, Long A, Tellides G, Avril S, Humphrey J, Bersi M (2022) Evolving mural defects, dilatation, and biomechanical dysfunction in angiotensin II-induced thoracic aortopathies. Arterioscler Thromb Vasc Biol 42(8):973–986. https://doi.org/10.1161/ATVBAHA.122.317394

35. Bellini C, Bersi MR, Caulk AW, Ferruzzi J, Milewicz DM, Ramirez F, Rifkin DB, Tellides G, Yanagisawa H, Humphrey JD (2017) Comparison of 10 murine models reveals a distinct biomechanical phenotype in thoracic aortic aneurysms. J R Soc Interface 14(130):1–8. https://doi.org/10.1098/rsif.2016.1036

36. Tezduyar TE, Takizawa K, Brummer T, Chen PR (2011) Space-time fluid–structure interaction modeling of patient-specific cerebral aneurysms. Int J Numer Methods Biomed Eng 27(11):1665–1710. https://doi.org/10.1002/cnm.1433

37. Tezduyar TE, Sathe S, Schwaab M, Conklin BS (2008) Arterial fluid mechanics modeling with the stabilized space-time fluid–structure interaction technique. Int J Numer Methods Fluids 57(5):601–629. https://doi.org/10.1002/fld.1633

38. Takizawa K, Tezduyar TE (2014) Fluid–structure interaction modeling of patient-specific cerebral aneurysms. In: Visualization and simulation of complex flows in biomedical engineering. Lecture notes in computational vision and biomechanics, vol 12. Springer, Dordrecht, pp. 25–45. https://doi.org/10.1007/978-94-007-7769-9

39. Takizawa K, Moorman C, Wright S, Purdue J, McPhail T, Chen PR, Warren J, Tezduyar TE (2011) Patient-specific arterial fluid–structure interaction modeling of cerebral aneurysms. Int J Numer Methods Fluids 65(1–3):308–323. https://doi.org/10.1002/fld.2360

40. Vignon-Clementel IE, Figueroa CA, Jansen KE, Taylor CA (2010) Outflow boundary conditions for 3D simulations of non-periodic blood flow and pressure fields in deformable arteries. Comput Methods Biomech Biomed Eng 13(5):625–640. https://doi.org/10.1080/10255840903413565

41. Xiao N, Alastruey J, Figueroa CA (2014) A systematic comparison between 1-D and 3-D hemodynamics in compliant arterial models. Int J Numer Methods Biomed Eng 30(2):204–231. https://doi.org/10.1002/cnm.2598

42. Olufsen MS (1999) Structured tree outflow condition for blood flow in larger systemic arteries. Am J Phys Heart Circul Phys 276(1):257–268. https://doi.org/10.1152/ajpheart.1999.276.1.H257

43. Petterson N, Sjoerdsma M, van Sambeek M, van de Vosse F, Lopata R (2021) Mechanical characterization of abdominal aortas using multi-perspective ultrasound imaging. J Mech Behav Biomed Mater 119:104509. https://doi.org/10.1016/j.jmbbm.2021.104509

44. Durbak E, Tarraf S, Gillespie C, Germano E, Cikach F, Blackstone E, Emerton K, Colbrunn R, Bellini C, Roselli EE (2021) *Ex-vivo* biaxial load testing analysis of aortic biomechanics demonstrates variation in elastic energy distribution across the aortic zone zero. J Thorac Cardiovasc Surg. https://doi.org/10.1016/j.jtcvs.2021.09.071

45. Chung J, Hulbert GM (1993) A time integration algorithm for structural dynamics with improved numerical dissipation: the generalized-α method. J Appl Mech 60(2):371–375. https://doi.org/10.1115/1.2900803

46. Valente R, Mourato A, Brito M, Xavier J, Tomás A, Avril S (2022) Fluid–structure interaction modeling of ascending thoracic aortic aneurysms in simvascular. Biomechanics 2:189–204. https://doi.org/10.3390/biomechanics2020016